Tellus
SERIES A
DYNAMIC
METEOROLOGY
AND OCEANOGRAPHY
PUBLISHED BY THE INTERNATIONAL METEOROLOGICAL INSTITUTE IN STOCKHOLM

*Tellus (2011), 63A, 223–237*





# Modelling of spatial variability and topographic effects over Arctic fjords in Svalbard

*By* TIINA KILPELÄINEN[1,2]*, TIMO VIHMA[3] and HARALDUR ÓLAFSSON[2,4], [1]*The University Centre in Svalbard, 9171 Longyearbyen, Norway*; [2]*Geophysical Institute, University of Bergen, Norway*; [3]*Finnish Meteorological Institute, Helsinki, Finland*; [4]*University of Iceland and Icelandic Meteorological Office, Reykjavik, Iceland*

(Manuscript 18 January 2010; in final form 21 July 2010)

ABSTRACT

The spatial variability of near-surface variables and turbulent surface fluxes was investigated in three Arctic fjords in Svalbard applying the Weather Research and Forecasting (WRF) mesoscale model. Ten real cases from winter and spring 2008, representing the most common large-scale flow directions, were simulated at 9, 3 and 1 km resolutions for 36 h each. Validation against tower observations and radiosoundings showed fairly good agreement, although a systematic warm and moist bias and slightly overestimated wind speeds were found close to the surface. The spatial variability within a fjord was large and it often reached levels comparable to the temporal variability. The spatial variability of the surface fluxes of sensible and latent heat was mostly controlled by the air and sea surface temperatures instead of wind speed. The same cases were also simulated without any topography over Svalbard. The topography increased the spatial variability but the influence on the mean values was not systematic, except that a clear warming effect was seen in all the fjords studied. The role of surface type increased with increasing air–sea temperature difference and was dominating over topographic effects for the air temperature, specific humidity and turbulent heat fluxes.

## 1. Introduction

Over Arctic fjords, as over ice-covered seas in general, the boundary conditions for the atmosphere are particular, as the surface conditions are controlled by sea ice dynamics and thermodynamics. The surface type may change rapidly due to advection of sea ice, while thermodynamic ice formation, growth and melt are slower processes. Ice-covered seas represent an extremely heterogeneous surface for most of the year; the surface temperature of the open water areas (cracks, leads and polynyas) is practically at the freezing point of sea water (−1.8 °C), while the surface temperature of thick, snow-covered ice floes in the central Arctic is sometimes less than −40 °C. Moreover, the turbulent surface fluxes can vary up to two orders of magnitude between the areas of open water and snow-covered sea ice.

The atmospheric boundary layer (ABL) over sea ice is usually stably stratified. The physics of the stable boundary layer (SBL) is poorly understood, and our knowledge is mostly based on observations of the mid-latitude nocturnal SBL. The SBL in polar regions is, however, long-living, which makes its structure even more complex, with close interaction of turbulence and gravity waves (Zilitinkevich and Esau, 2005). Numerical weather prediction (NWP) and climate models usually have their largest errors in the SBL (Hunt et al., 1996; Poulos and Burns, 2003). Over sea ice, modelling of the ABL is further complicated by the localized convection over leads and polynyas (Lüpkes et al., 2008), and models often suffer from the lack of accurate information of the sea ice concentration (Valkonen et al., 2008). Hence, large errors in the near-surface variables and surface fluxes are common over sea ice in NWP models (Tisler et al., 2008), reanalyses (Curry et al., 2002; Vihma et al., 2002) and climate models (Tjernström et al., 2005).

Furthermore, the ABL processes over Arctic fjords are strongly influenced by the complex topography. Due to strong stratification, non-linear effects on flows across topography at high latitudes are comparable to the non-linear effects on flows across much higher topography elsewhere in the world (Skeie and Grns, 2000). In general, the topographic effects may include channelling, drainage flows and mountain waves (Barry, 2008). Modelling of these features in the case of small-scale topography requires very high resolution. For example, Valkonen et al. (2010) applied a horizontal resolution of 0.9 km to simulate gravity waves generated by an Antarctic nunatak. Little research has so far been undertaken on the modelling of topographically influenced ABL over sea ice. Heinemann (2003) concluded based on a modelling study that the synoptically forced katabatic

*Corresponding author.
e-mail: tiina.kilpelainen@unis.no
DOI: 10.1111/j.1600-0870.2010.00481.x

winds could result in a fast formation of a coastal polynya in East Greenland. Flows off Greenland have also been studied by Heinemann and Klein (2002), Klein et al. (2001, 2002). Research aircraft campaigns associated with mesoscale modelling have been carried out over Svalbard and its surroundings. Vihma et al. (2003) modelled the ABL over Storfjorden (Fig. 1) and Vihma et al. (2005) over the sea ice south of Nordaustlandet (Fig. 1), but in both these studies the flow conditions were such that no significant topographic effects on the ABL were detected. Sandvik and Furevik (2002) applied the mesoscale model MM5 over Svalbard and compared the results against scatterometer-based winds, which restricted their analyses to the open sea.

In several modelling studies, for example, related to stratified flows (Skeie and Grønås, 2000) and reverse tip jets (Ohigashi and Moore, 2009), jets have been found to radiate out of fjords in Svalbard and Greenland. However, only a few studies have specifically addressed the ABL in a fjord environment. Argentini et al. (2003) made tethersonde soundings on the coast of Kongsfjorden, Svalbard (Fig. 1), and concluded that the ABL over the fjord was strongly influenced by the topography and winds of local origin such as katabatic winds. Kilpeläinen and Sjöblom (2010) analysed turbulence and profile data from a 30-m tower on the shore of Isfjorden (Fig. 1), and concluded that the momentum and sensible heat exchange in a fjord system differed from the exchange taking place over the open ocean mainly due to topographic effects. They also found that the Monin–Obukhov similarity theory, widely applied in atmospheric models, was applicable when the flow was along the fjord with moderate or high wind speeds.

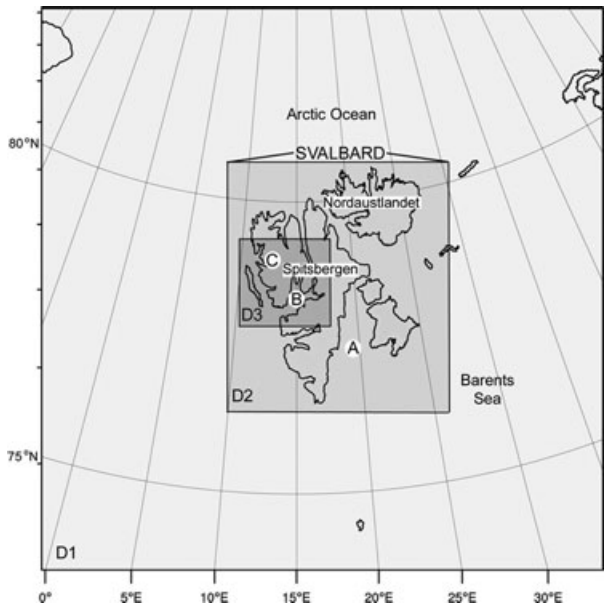


*Fig. 1.* Domains D1, D2 and D3, used in WRF model, with resolutions of 9, 3 and 1 km, respectively. The studied fjords are: (A) Storfjorden, (B) Isfjorden and (C) Kongsfjorden.

This study addresses the spatial variability of the near-surface variables and turbulent surface fluxes over Svalbard fjords, particularly Isfjorden, Kongsfjorden and Storfjorden. These three fjords have different size, shape and orientation, allowing diagnosis on the effects of these parameters on the ABL. The Weather Research and Forecasting (WRF) mesoscale model is applied in high-resolution simulations, which are described in Section 2. Partly ice-covered fjords surrounded by mountains are naturally of academic interest as an extremely challenging modelling environment, but the modelling also has practical importance. Information on the meteorological variables over fjords is needed for operational weather services for the general public and specifically for aviation, navigation and fisheries. Moreover, quantification of the near-surface variables and the turbulent surface fluxes over fjords is necessary in climate-related studies, for example, to provide realistic boundary conditions for ocean models simulating the circulation (Skogseth et al., 2007) and the deep water formation in fjords (Skogseth et al., 2008), some of which (e.g. Storfjorden) being important even for the global ocean circulation. The main objectives of this study are to distinguish the most important factors controlling the spatial variability and compare the level of spatial and temporal variability within a fjord; the results from these are presented in Section 3. The effects of topography and surface types (sea ice and open water) on the spatial variability are analysed separately. To distinguish between the thermodynamic and topographic effects in fjords, 10 real weather situations are simulated (a) with realistic topography and (b) without any topography over Svalbard, that is, with flat islands. The cases modelled are from winter and spring, when the thermal contrast between the open sea and snow/ice surfaces is large. To understand the role of thermodynamics even in more detail, sensitivity simulations without sea ice and with the entire fjords covered by sea ice are also made. Discussion on the results follows in Section 4.

## 2. Model simulations

### *2.1. The model setup*

The simulations were made using the Advanced Research WRF (ARW) model, version 3.0.1.1, developed by the National Center for Atmospheric Research (NCAR). The ARW consists of fully compressible non-hydrostatic equations using terrain-following hydrostatic-pressure vertical coordinate. For further details of the model, see Skamarock et al. (2008).

Three one-way nested polar stereographic domains at horizontal resolutions of 9, 3 and 1 km, shown in Fig. 1, were used in the simulations. The outer domain D1 (120 × 120 grid points), centred at 78.5°N, 17.0°E, covers a large area from the northeast corner of Greenland in the west to Franz Josef Land in the east. The middle domain D2 (130 × 154 grid points), covers tightly the archipelago of Svalbard, including Storfjorden, at 3 km resolution. The inner domain D3 (163 × 175 grid points), covers

the two smaller fjords, Isfjorden and Kongsfjorden, situated on the west coast of the largest island of the archipelago, Spitsbergen, and captures the complex topography around them at 1 km resolution. In all domains, the model has 62 levels in vertical, of which 19 are in the lowest 1000 m of the atmosphere; the lowest full model level is at 36 m. The model top was set to 50 hPa. The model was initialized by the European Centre for Medium-Range Weather Forecasts (ECMWF) operational analysis with 0.5° horizontal resolution, and the lateral boundary conditions were given at 6-h intervals during the simulation. Time steps of 54 s (for D1), 18 s (for D2) and 6 s (for D3) were applied.

The WRF model includes numerous options for subgrid-scale physical parametrizations, hereafter called as physics options. In this study, these are chosen following Hines and Bromwich (2008), who compared several combinations of physics options for the Greenland ice sheet. However, their physics options included polar modifications to the standard WRF, which are not used in this study. The best combination of Hines and Bromwich (2008) has also shown good agreement with observations over the Arctic ice pack (Bromwich et al., 2009). Hence, long-wave radiation is parametrized with the Rapid Radiative Transfer Model (RRTM) (Mlawer et al., 1997) and short-wave radiation with the Goddard scheme (Chou and Suarez, 1994). Cloud microphysics is parametrized with the Single-Moment 5-class scheme which includes prognostic equations for vapour, rain, snow, cloud ice and cloud water (Hong et al., 2004). The Mellor–Yamada–Janjic (MYJ) scheme, which is a level 2.5 closure model for turbulence, was chosen for the boundary layer, and is run in conjunction with the Eta surface layer scheme (Janjic, 1996, 2002). The Eta surface layer scheme is based on the Monin–Obukhov similarity theory and the surface fluxes over water surfaces are computed by an iterative method. The surface fluxes over land and sea ice are provided by the Noah Land Surface Model (LSM) (Chen and Dudhia, 2001), which is a 4-layer soil temperature and moisture model with snow cover prediction. The Grell–Devenyi ensemble cumulus scheme (Grell and Dévényi, 2002) is applied for the outermost domain.

The sea ice and surface temperature fields of the ECMWF operational analyses were compared against the daily sea ice charts produced by the Norwegian Meteorological Institute and visual observations. Errors were found in the ECMWF fields in fjords and near coastlines. Hence, the sea ice and sea surface temperature fields in the fjords studied were manually corrected and set consistent with each other. During the simulations, Storfjorden was fully covered with sea ice, whereas Isfjorden and Kongsfjorden had sea ice only in their inner parts (Fig. 2). The sea surface temperature was set to $-1.75$ °C in the ice-free parts of the fjords. The sea ice thickness was 3 m, which is the standard value in the Noah LSM. The thermodynamic effects of the excessive sea ice thickness were compensated by the fact that the snow thickness in WRF (0.05 m) was lower than in reality (some 0.2 m).

### 2.2. *Simulation strategy*

Based on the NCEP/NCAR Reanalysis at 850 hPa, the five most common large-scale wind directions over Svalbard in January–May 2008, representing approximately 80% of all cases, were southeast (SE), east (E), northeast (NE), north (N) and northwest (NW). These five main directions were chosen for simulations of spatial variability in the three fjords

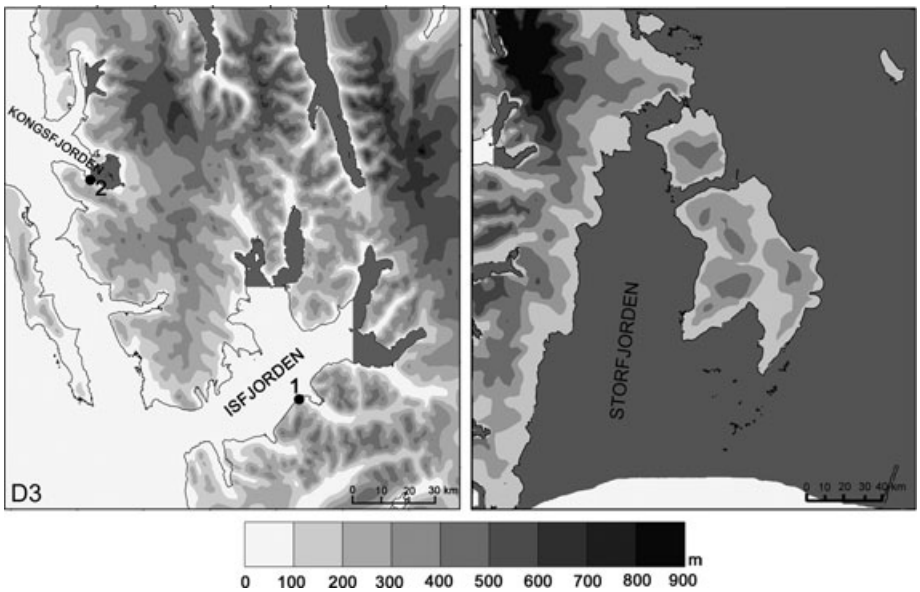


*Fig. 2.* Terrain height and sea ice cover (dark grey) in Isfjorden (left-hand panel), Kongsfjorden (left-hand panel) and Storfjorden (right-hand panel). The locations of observation sites in Isfjorden (1) and Kongsfjorden (2) are shown on the map (left-hand panel).

(Storfjorden, Isfjorden and Kongsfjorden) (Fig. 1). This study mainly consists of two types of simulations. First, 10 real cases from winter and spring 2008, two per each selected large-scale wind direction, were simulated and these simulations are termed as 'CONTROL'. The dates and wind directions of cases were 19 February NW, 7 April NW, 14 February N, 29 March N, 13 February NE, 18 March NE, 24 February E, 4 March E, 26 February SE and 12 March SE. All the selected cases had a relatively uniform geostrophic flow field over Svalbard with moderate or high wind speeds. Each of the simulations was 36 h long including 12 h of spin-up time. Second, the same 10 cases were simulated with the topography of Svalbard set to sea level, and these simulations are termed as 'NOTOPO'. Other factors, like surface characteristics, were not changed in the NOTOPO simulations; hence, the differences between the CONTROL and NOTOPO results indicate the influence of the surrounding topography on the local meteorological conditions. In addition, to analyse the impact of surface type in more detail, two of the cases (19 February NW and 12 March SE) were simulated without any sea ice cover and with the entire fjords covered by sea ice. These simulations are termed as 'NOICE' and 'FULLICE', respectively. The selected cases represent very different thermal conditions; the NW case was cold and the thermal contrasts were large and the SE case, in turn, was the warmest of the 10 cases simulated.

### 2.3. Model validation

The model results for near-surface variables were compared with tower measurements taken on the coast of Isfjorden (78°15′N, 15°24′E) and on the coast of Kongsfjorden (78°55′N, 11°55′E) (Fig. 2). Moreover, 16 rawinsonde (DigiCORAIII, Vaisala) profiles from the coast of Kongsfjorden, measured by the Alfred Wegener Institute (AWI), were used for the validation (Fig. 2).

At the measurement site on the coast of Isfjorden, slow-response measurements of wind speed (A100LK, Vector instruments), temperature and relative humidity (HMP45AC, Vaisala) were taken. The height of the tower measurements, used in this study, was 10 m (above the ground). As the tower was located only 30 m from the shoreline, observations during wind directions from a 165° wide sector (from southwest (SW) clockwise to NE) represented conditions over the fjord. Outside this sector the flow originated from land. The tower measurements were averaged over 30 min. More detailed description of the tower measurements on the coast of Isfjorden and the data analysis is given in Kilpeläinen and Sjöblom (2010). From Kongsfjorden, AWI tower measurements of 10-m wind speed (Combined wind sensor, Thiess), 2-m temperature (PT-100, ventilated) and 2-m relative humidity (HMP230) were used. These measurements were averaged over 60 min. The tower was located a few hundreds of metres from the shoreline, winds from the sector from NW clockwise to SE representing a flow from the fjord.

The model values from the CONTROL simulations were taken from the grid point closest to the observation site. To be comparable with the measurements at Isfjorden, the simulated temperature and humidity were interpolated to the height of 10 m using an algorithm that accounts for the stability and roughness effects on the vertical profiles (Launiainen and Vihma, 1990). The iterative algorithm is based on the Monin–Obukhov theory. It applies the stability functions of Holtslag and de Bruin (1988) for stably stratified conditions and those of Högström (1988) for convective conditions. The roughness length for heat and moisture is calculated according to Andreas (1987).

The root-mean-square (RMS) error and bias for wind speed, temperature and humidity from Isfjorden and Kongsfjorden, calculated as the observation subtracted from the modelled value, are shown in Table 1. The error estimates are shown both for all the cases together and for each large-scale flow direction separately (the observations were averaged over 30 or 60 min but the modelled values were instant values). The biases for wind speed (Table 1) were generally positive, ranging from 0.6 to 1.3 m $s^{-1}$ in Isfjorden and from 0.7 to 3.1 m $s^{-1}$ in Kongsfjorden. An exception was the SE direction in Isfjorden, associated with a bias of 6.8 m $s^{-1}$. In these cases the simulated winds were strong, ranging from 13 to 19 m $s^{-1}$. Thus, the model clearly overpredicted wind speeds in the cases of SE flows entering the fjord from a large valley orientated in the SE–NW direction. The biases for temperature were also positive and largest for the N and NE flows, when the air temperature was often lowest. The RMS errors were small when temperature was above −10 °C. Except for the E flows in Isfjorden, specific humidity had positive biases for all large-scale flow directions. The coastal location of the measurement sites made the results very sensitive to wind direction and even small differences in wind direction could therefore lead to large differences in other variables. However, the RMS errors were relatively small when both observed and simulated flows originated from the fjord.

Figure 3 shows the mean observed profiles of wind speed, air temperature and specific humidity as well as the model biases and RMS errors of the profiles interpolated to the model levels in Kongsfjorden. All the biases were positive, except for temperature above 800 m. Wind speed and temperature had their largest RMS errors close to the surface but specific humidity had also a peak at a higher altitude. The large differences near the surface, especially in case of wind speed, can probably be explained by the very complex topography around the measuring site on the coast of Kongsfjorden that could not be resolved by the model.

## 3. Results

### 3.1. Spatial variability

Figure 4 shows the turbulent surface flux fields in two of the fjords studied, Isfjorden and Kongsfjorden, during an E flow. In this example case, the maximum fluxes lay over the open water in

*Table 1.* The bias and RMS error (RMSE) of simulated near-surface wind speed $U$, air temperature $T$ and specific humidity $q$ in Isfjorden (78°15′N, 15°24′E) and Kongsfjorden (78°55′N, 11°55′E) for different large-scale flow directions. $N$ indicates the number of values and $n$ the number of cases used in the calculations. Observed mean and standard deviation are given for each case separately

| | | | ISFJORDEN | | | | KONGSFJORDEN | | | |
|---|---|---|---|---|---|---|---|---|---|---|
| Variable | Flow direction | $N(n)$ | Mean($SD$) case 1 | Mean($SD$) case 2 | **bias** | **RMSE** | Mean($SD$) case 1 | Mean($SD$) case 2 | **bias** | **RMSE** |
| $U$ (m s$^{-1}$), 10 m | ALL | 250 (10) | | | **2.3** | **3.2** | | | **2.1** | **2.6** |
| | NW | 50 (2) | 4.6 (1.1) | 4.7 (1.8) | **1.0** | **2.6** | 3.2 (1.7) | 3.0 (0.6) | **0.7** | **0.9** |
| | N | 50 (2) | 6.6 (2.3) | 2.0 (1.0) | **1.2** | **2.5** | 5.1 (2.5) | 6.5 (2.7) | **2.1** | **2.5** |
| | NE | 50 (2) | 8.8 (1.5) | 4.3 (0.7) | **0.6** | **2.0** | 6.5 (1.4) | 2.7 (0.6) | **3.1** | **3.6** |
| | E | 50 (2) | 7.8 (1.5) | 9.9 (1.9) | **1.3** | **2.1** | 7.5 (1.3) | 1.9 (0.5)) | **2.7** | **3.0** |
| | SE | 50 (2) | 10.5 (1.9) | 7.2 (1.0) | **6.8** | **6.8** | 11.4 (1.6) | 2.6 (0.7) | **2.1** | **3.2** |
| $T$ (°C) | ALL | 250 (10) | | | **1.5** | **1.9** | | | **3.0** | **4.0** |
| (Isfjorden 10 m, | NW | 50 (2) | −13.3 (2.4) | −4.9 (1.7) | **0.6** | **1.5** | −15.1 (1.4) | −5.1 (1.1) | **3.2** | **3.6** |
| Kongsfjorden 2 m) | N | 50 (2) | −13.1 (0.8) | −13.5 (0.7) | **2.4** | **2.5** | −15.7 (1.1) | −14.0 (1.3) | **4.1** | **5.6** |
| | NE | 50 (2) | −11.0 (1.2) | −15.6 (0.5) | **2.6** | **3.3** | −12.9 (1.8) | −16.7 (0.9) | **3.7** | **4.5** |
| | E | 50 (2) | −10.9 (2.2) | −13.2 (0.4) | **1.7** | **1.9** | −11.7 (1.0) | −12.3 (1.3) | **0.6** | **2.5** |
| | SE | 50 (2) | −8.4 (0.6) | −3.1 (0.4) | **0.1** | **0.3** | −7.4 (0.9) | −6.6 (0.5) | **3.2** | **4.0** |
| $q$ (g kg$^{-1}$) | ALL | 250 (10) | | | **0.16** | **0.21** | | | **0.22** | **0.28** |
| (Isfjorden 10 m, | NW | 50 (2) | 0.88 (0.18) | 1.84 (0.22) | **0.27** | **0.28** | 0.81 (0.12) | 2.3 (0.26) | **0.15** | **0.17** |
| Kongsfjorden 2 m) | N | 50 (2) | 0.79 (0.04) | 0.88 (0.12) | **0.22** | **0.23** | 0.71 (0.06) | 0.80 (0.08) | **0.21** | **0.22** |
| | NE | 50 (2) | 0.96 (0.13) | 0.68 (0.05) | **0.20** | **0.20** | 0.79 (0.18) | 0.55 (0.03) | **0.18** | **0.23** |
| | E | 50 (2) | 1.10 (0.35) | 0.96 (0.22) | **−0.06** | **0.17** | 0.86 (0.11) | 0.69 (0.10) | **0.39** | **0.44** |
| | SE | 50 (2) | 1.23 (0.16) | 1.9 (0.07) | **0.16** | **0.19** | 1.3 (0.12) | 1.5 (0.30) | **0.28** | **0.36** |

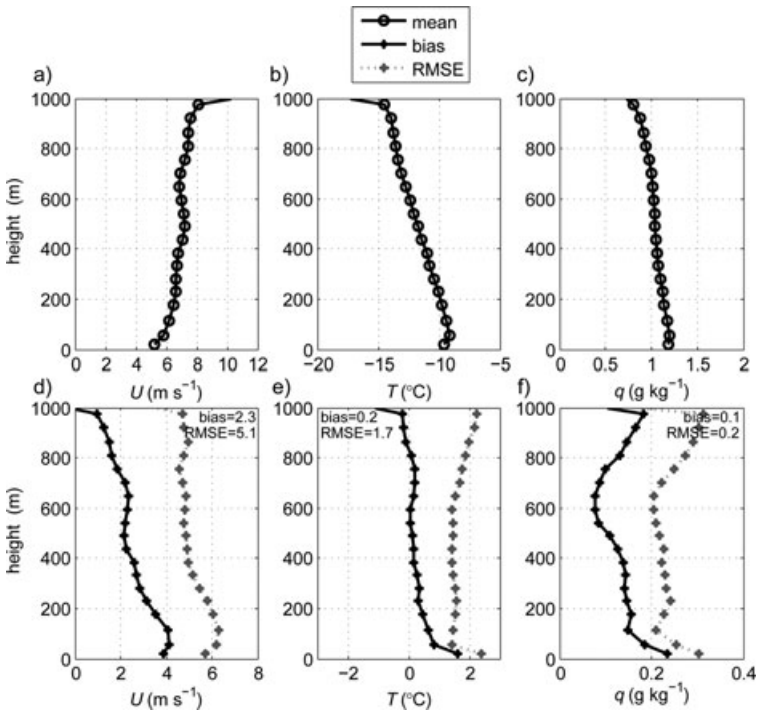


*Fig. 3.* The mean observed profiles of (a) wind speed $U$, (b) air temperature $T$ and (c) specific humidity $q$ on the coast of Kongsfjorden (78°55′N, 11°55′E), based on 16 rawinsonde observations, and bias and RMS error (RMSE) of simulated vertical profiles of (d) wind speed $U$, (e) air temperature $T$ and (f) specific humidity $q$. The numerical values show the bias and RMSE averaged over the whole profile.

the eastern part of Isfjorden, where the flow originating from land and sea ice first met the open sea. The plumes of cold air did not spread all over Isfjorden which increased the spatial variability of the sensible heat flux. Furthermore, some areas on the southern coast of Isfjorden as well as in the northern branch of Isfjorden seemed to be sheltered by the topography, which led to weaker winds and smaller fluxes. The spatial variability of the turbulent fluxes within Isfjorden was extreme; the range of variability was

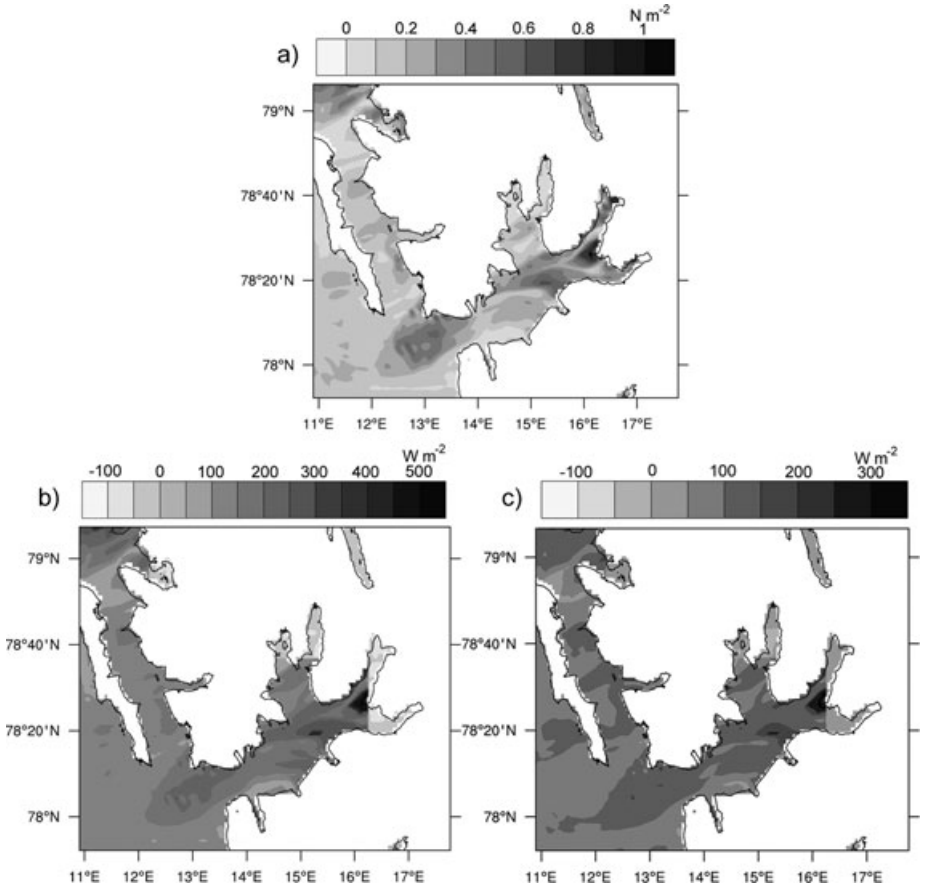


*Fig. 4.* Turbulent surface fluxes of (a) momentum $\tau$, (b) sensible heat $H$ and (c) latent heat $LE$ in Isfjorden and Kongsfjorden for an easterly flow on 24 February 2008 at 14 UTC. The land area is masked out.

1 N m$^{-2}$ for the momentum flux, 600 W m$^{-2}$ for the sensible heat flux, and 300 W m$^{-2}$ for the latent heat flux. The variability was also significant in Kongsfjorden although the absolute values were smaller. In Storfjorden, which was fully covered with sea ice, the turbulent heat fluxes had smaller magnitudes but as an example case shown in Fig. 5 demonstrates, the variability was significant compared to the mean fluxes. The range of variability was approximately 1 N m$^{-2}$ for the momentum flux, 100 W m$^{-2}$ for the sensible heat flux, and 40 W m$^{-2}$ for the latent heat flux.

Statistical analyses were made to investigate the amount of variability, the effects of large-scale flow directions and differences between the studied fjords. The 10-m wind speed, 2-m temperature and specific humidity as well as the turbulent surface fluxes at each grid point were averaged over the simulation length (24 h), and the spatial mean and the standard deviation, as well as the minimum and maximum values were calculated for the whole fjord area. The results for Storfjorden, Isfjorden and Kongsfjorden are shown in Figs 6–8, respectively. Because a large portion of the total variation in fjords is caused by the different surface types, the areas of open water and sea ice cover were also considered separately. The horizontal resolution used in the calculations was 1 km for Isfjorden and Kongsfjorden, and 3 km for Storfjorden, and the number of grid points in each area is given in Table 2. In addition, multiple regression analyses were made to find out (a) which factors control the temporal variability of the spatial standard deviation of wind speed, temperature, specific humidity and the surface fluxes and (b) which factors control the spatial variability of the temporally averaged surface fluxes in each fjord.

In all three fjords, wind speeds (Figs 6a–8a) varied considerably in space. Some dependency on the large-scale flow direction could be seen in Kongsfjorden, where the standard deviation of wind speed (Fig. 8) was somewhat larger for the E and NE flows. This large variability was caused by several different effects in Kongsfjorden; a strong blocking effect, causing weaker winds, occurred on the southwestern coast during an E flow and some sheltering effects were found on the sides of the fjord when the E or NE flows were turned to follow the shape of the fjord. In Storfjorden and Isfjorden instead, the standard deviation and the range did not clearly depend on the large-scale flow direction. Stepwise multiple regression analysis revealed that the normalized standard deviation (standard deviation divided by the mean) of wind speed had statistically significant dependence on the mean wind speed: averaged over all the fjords studied, the

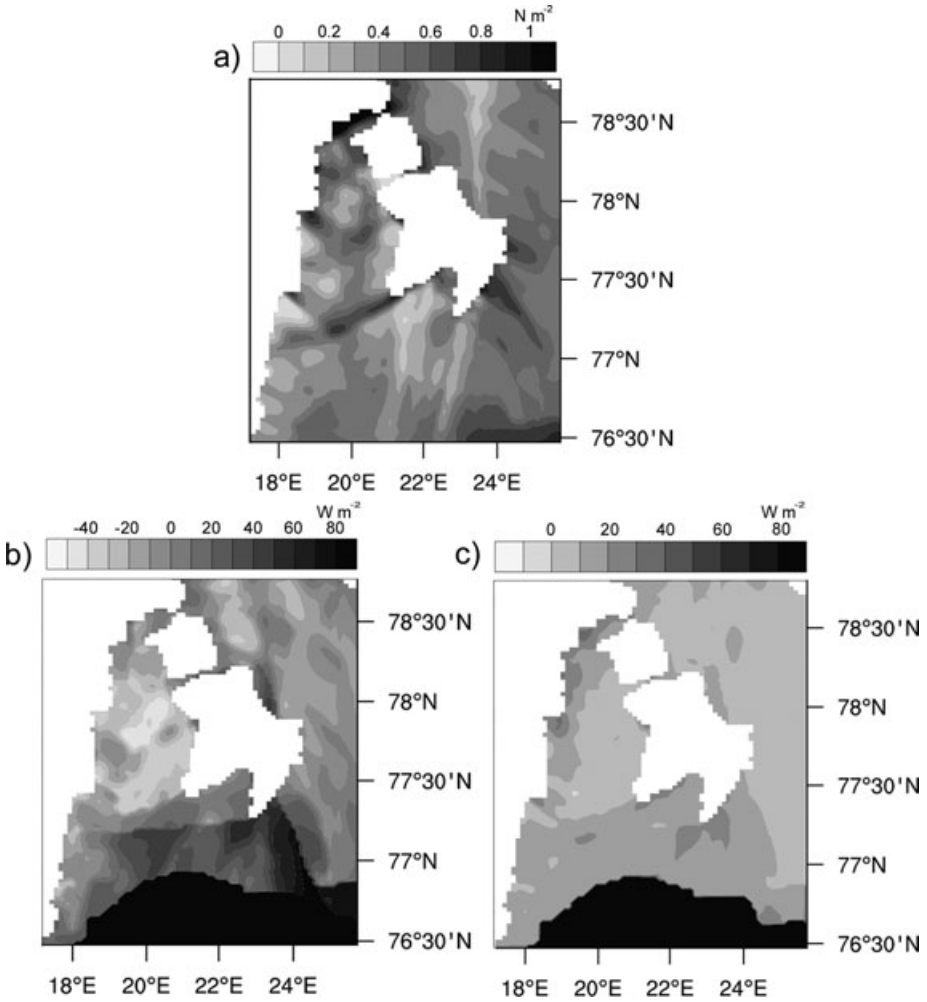


*Fig. 5.* Turbulent surface fluxes of (a) momentum $\tau$, (b) sensible heat $H$ and (c) latent heat $LE$ in Storfjorden for a northeasterly flow on 13 February 2008 at 12 UTC. The land area is masked out.

correlation coefficient was $r = -0.71 (p < 0.05)$. In Isfjorden and Kongsfjorden, an improved correlation coefficient of—0.90 ($p < 0.01$) was reached, when both the mean wind speed and the spatial standard deviation of specific humidity were included as explaining variables.

2-m temperatures did not show distinct amount of spatial variability for any flow direction in Kongsfjorden (Fig. 8b), except due to different surface types, but some dependency on the flow direction could be seen in the two largest fjords (Figs 6b–7b). Over the open water area in Isfjorden, the standard deviation of temperature was largest for the NE flows, when cold air was able to enter the fjord from the northern branches, but the plumes of cold air were not spreading efficiently all over the fjord. In Storfjorden, the standard deviation was slightly larger for the NW flows, when relatively warm air originating from the open ocean off the western coast of the largest island, Spitsbergen (Fig. 1), met the cold air mass in the eastern part of Storfjorden. The standard deviation was also large for a SE flow, when relatively warm air in the southern part of Storfjorden originated from the SE direction but air in the northern part of the fjord entered from the N due to a blocking effect of the mountains, and was relatively cold due to a long fetch over the sea ice. In Isfjorden and Kongsfjorden, the temporal variability of the normalized spatial standard deviation of air temperature was controlled by the mean temperature; the variability increased with decreasing mean temperature ($r = -0.72$, $p < 0.05$).

The mean air specific humidity (Figs 6c–8c) was very small in all winter cases simulated, and the variability over a fjord was dominantly caused by the different surface types. In only one of the cases, which was also the warmest, specific humidity showed pronounced variability in the two largest fjords. In Storfjorden, the temporal variability of the normalized spatial standard deviation of specific humidity was controlled by the standard deviation of air temperature ($r = -0.68$, $p < 0.05$). In Isfjorden, the controlling factor was the mean air temperature ($r = -0.73$, $p < 0.05$).

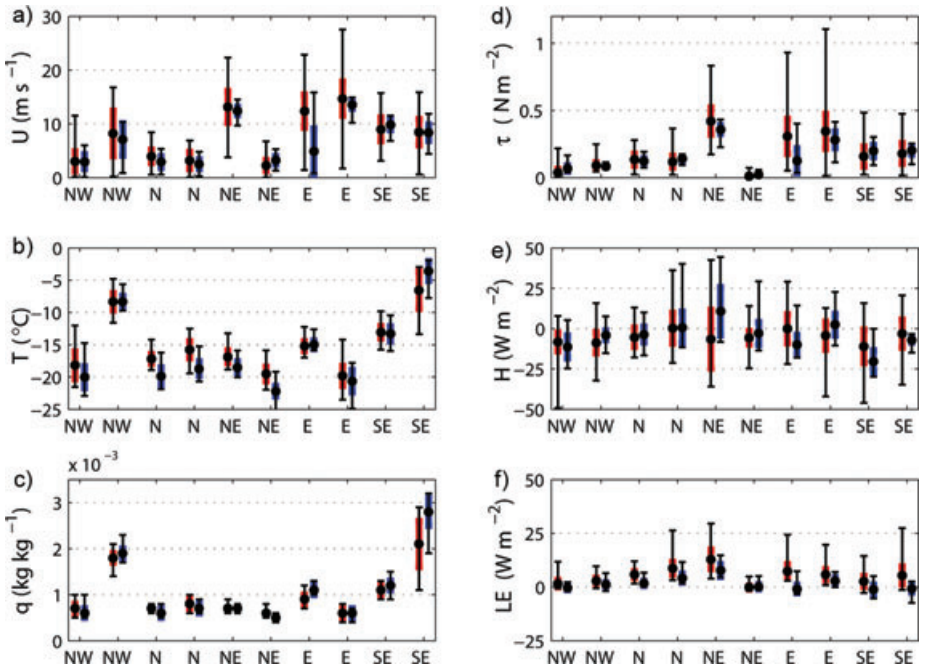


*Fig. 6*. Statistical values for (a) 10-m wind speed $U$, (b) 2-m temperature $T$, (c) 2-m specific humidity $q$, (d) the momentum flux $\tau$, (e) the sensible heat flux $H$ and (f) the latent heat flux $LE$ for Storfjorden simulated at 3 km horizontal resolution. In each case, the values for the CONTROL simulations are on the left-hand side and the values for the NOTOPO simulations on the right-hand side. The dots denote the mean values, the thick bars the standard deviation, and the thin bars the minimum and maximum values, i.e. the range. The dates are in the order given in Section 2.2.

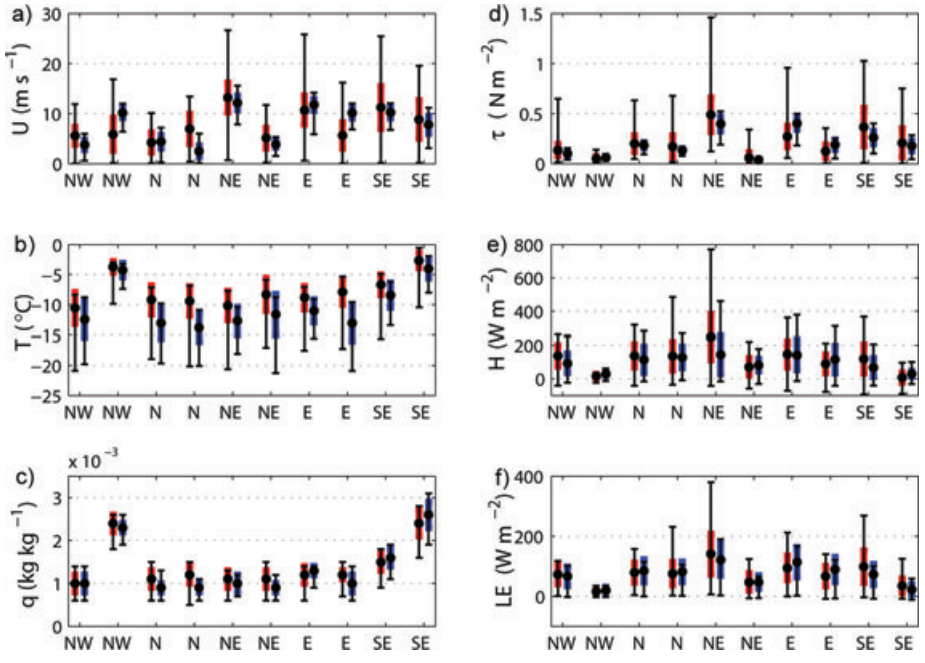


*Fig. 7*. Same as in Fig. 6 but for Isfjorden at 1 km horizontal resolution.

The momentum flux (Figs 6d–8d) had a relatively large range in all the fjords, except for a few cases with an almost uniform momentum flux field in Kongsfjorden. Although the orientations of the fjords studied are different, the flow directions causing the largest variability were mainly the same for all the fjords; the standard deviation of the momentum flux was largest for the NE, E and SE flows. The spatial variations of the temporally averaged momentum flux at each grid point were controlled by the

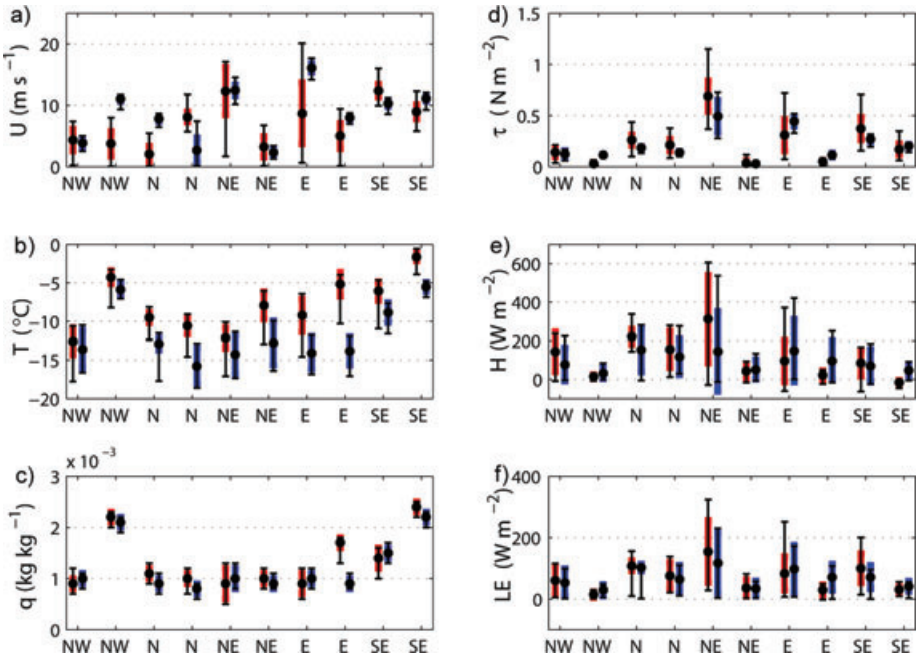


*Fig. 8.* Same as in Fig. 6 but for Kongsfjorden at 1 km horizontal resolution.

*Table 2.* Spatial (SPAT) and temporal (TEMP) standard deviations and their ratios for simulated 10-m wind speed $U$, 2-m temperature $T$, 2-m specific humidity $q$, the momentum flux $\tau$, the sensible heat flux $H$ and the latent heat flux $LE$ in Storfjorden (SF), Isfjorden (IF), and Kongsfjorden (KF) for the CONTROL simulations. The number of grid points is given under the name

| | | SF fjord 1290 | IF fjord 3223 | IF water 2684 | IF ice 539 | KF fjord 277 | KF water 157 | KF ice 120 |
|---|---|---|---|---|---|---|---|---|
| SPAT($U$) | (m s$^{-1}$) | 2.4 | 2.8 | 2.6 | 3.2 | 2.1 | 1.5 | 2.1 |
| TEMP($U$) | (m s$^{-1}$) | 4.6 | 3.1 | 2.9 | 4.0 | 3.7 | 3.9 | 4.1 |
| **SPAT(U)/TEMP(U)** | | **0.52** | **0.90** | **0.90** | **0.80** | **0.57** | **0.38** | **0.51** |
| SPAT($T$) | (°C) | 1.4 | 2.0 | 0.8 | 1.2 | 1.3 | 0.4 | 0.4 |
| TEMP($T$) | (°C) | 4.5 | 2.7 | 2.4 | 3.9 | 3.6 | 3.3 | 3.8 |
| **SPAT(T)/TEMP(T)** | | **0.31** | **0.74** | **0.33** | **0.31** | **0.36** | **0.12** | **0.11** |
| SPAT($q$) | (g kg$^{-1}$) | 0.11 | 0.20 | 0.14 | 0.08 | 0.14 | 0.04 | 0.04 |
| TEMP($q$) | (g kg$^{-1}$) | 0.5 | 0.5 | 0.5 | 0.5 | 0.6 | 0.5 | 0.6 |
| **SPAT(q)/TEMP(q)** | | **0.22** | **0.40** | **0.28** | **0.13** | **0.28** | **0.07** | **0.07** |
| SPAT($\tau$) | (N m$^{-2}$) | 0.06 | 0.10 | 0.09 | 0.12 | 0.07 | 0.05 | 0.06 |
| TEMP($\tau$) | (N m$^{-2}$) | 0.14 | 0.14 | 0.13 | 0.17 | 0.20 | 0.20 | 0.20 |
| **SPAT($\tau$)/TEMP($\tau$)** | | **0.43** | **0.71** | **0.69** | **0.71** | **0.35** | **0.25** | **0.30** |
| SPAT($H$) | (W m$^{-2}$) | 8.6 | 66.1 | 43.3 | 13.5 | 72.4 | 25.8 | 5.5 |
| TEMP($H$) | (W m$^{-2}$) | 3.6 | 69.7 | 79.1 | 15.0 | 102.1 | 141.5 | 64.3 |
| **SPAT(H)/TEMP(H)** | | **2.39** | **0.95** | **0.55** | **0.90** | **0.71** | **0.18** | **0.09** |
| SPAT($LE$) | (W m$^{-2}$) | 2.5 | 35.8 | 22.9 | 6.2 | 37.6 | 13.8 | 3.9 |
| TEMP($LE$) | (W m$^{-2}$) | 3.8 | 35.2 | 41.0 | 7.6 | 43.8 | 23.4 | 13.2 |
| **SPAT(LE)/TEMP(LE)** | | **0.66** | **1.02** | **0.56** | **0.82** | **0.86** | **0.59** | **0.30** |

wind speed and over the open water also by the air temperature. Considering the temporal variability of the normalized spatial standard deviation, over the sea ice covered area of Kongsfjorden the variability in the momentum flux was controlled by the normalized spatial standard deviation of mean wind speed ($r = 0.68$, $p < 0.05$), whereas over the whole Isfjorden the controlling factor was the normalized spatial standard deviation of the surface temperature ($r = 0.67$, $p < 0.05$). The latter

demonstrates the strong effects of stratification on the momentum flux; although the flux is parametrized as a function of the square of the wind speed, the standard deviation was not controlled by the wind speed but by the stratification effect on the drag coefficient.

For the sensible heat flux (Figs 6e–8e), the NE and SE flows generally caused the largest variability on a single surface type in all the fjords, regardless of their orientation. In addition, the spatial variability due to the different surface types was significant. The spatial variations of the temporally averaged sensible heat flux in all the fjords studied were strongly controlled by the air temperature, sea-surface temperature and their difference. In Isfjorden and Kongsfjorden, the temporal variability of the normalized spatial standard deviation of the sensible heat flux was controlled by the normalized spatial standard deviation of the air temperature and in Isfjorden also by the mean sea surface temperature.

The standard deviation and the range of latent heat flux (Figs 6f–8f) were evidently dependent on the flow direction. In all the three fjords, the spatial variability of latent heat flux was reduced for the NW flows. As in the case of the sensible heat flux, the spatial variations of the temporally averaged flux were mainly controlled by the air temperature, sea-surface temperature and their difference. However, the wind speed was occasionally the dominating factor in Isfjorden and Kongsfjorden.

### 3.2. Sensitivity to horizontal resolution

Results from the CONTROL simulations at 1, 3 and 9 km resolutions (only at 3 and 9 km for Storfjorden) were compared. In several cases the results at the coarser resolutions deviated largely from the results at the highest resolution. On average, the coarser resolutions decreased the mean wind speed by 1–2 m s$^{-1}$ in Storfjorden and Isfjorden, but increased it in Kongsfjorden. The magnitude and sign of the mean temperature deviations varied noticeably between the fjords and surface types, and the range was typically $\pm$ 3 °C. The deviations in the mean turbulent fluxes were largest in Kongsfjorden, where the mean heat fluxes differed by up to 50 W m$^{-2}$. In Isfjorden, the standard deviation of air temperature was 0.3–1.2 °C larger at 9 km resolution than at 1 km. For other fjords and variables, the effect of coarser resolution on the standard deviations varied largely. Thus, the effect of the coarser resolution was systematic neither for any of the variable means nor the standard deviations, and even the sign of the deviations varied from case to case.

### 3.3. Topographic effects

Figures 6–8 show the statistical values for both the CONTROL simulations and NOTOPO simulations, and their comparison reveals the impact of topography. The standard deviations as well as the ranges were generally reduced in the NOTOPO simulations, especially in Kongsfjorden, and also the mean values were affected. The influence of topography was different for each variable.

The surrounding topography seemed to slightly increase the mean wind speed in Storfjorden, but to more commonly decrease it in Kongsfjorden, especially for the E flows. In Isfjorden, the effect of topography on the mean wind speed was not consistent. Figs 6–8 strongly indicate that the surrounding topography had a warming effect in all the fjords studied, and the magnitude of the effect increased with decreasing fjord size; the mean warming effect was approximately 1 °C in Storfjorden, 3 °C in Isfjorden and 4 °C in Kongsfjorden. In contrast to the other variables, the standard deviation and the range of temperature were not notably smaller in the NOTOPO simulations. The effect of topography on the specific humidity was generally small, although a decreasing effect could be seen particularly for the SE flows.

The effect of the topography on the momentum flux was not consistent for any fjord, surface type or large-scale flow direction. The sensible heat flux had higher mean values in the NOTOPO than CONTROL simulations over the open water areas, which was closely linked to lower temperatures in the NOTOPO simulations. Over the sea ice covered areas, the downward sensible heat flux increased (more negative) when the topography was present and occasionally even the sign of the flux was different between the two simulation types. The topography increased the latent heat flux in the whole fjords as well as over the sea ice covered areas, but the effect was not consistent in the open water areas. The topography had different effect on the sensible and latent heat fluxes, because the main factors controlling the local fluxes were partly different as described in Section 3.1.

The bulk Richardson number ($Ri$) was calculated from the modelled wind speeds and potential temperatures as follows:

$$Ri = \frac{g}{0.5(\theta_i + \theta_{i+1})} \frac{\theta_{i+1} - \theta_i}{(u_{i+1} - u_i)^2} (z_{i+1} - z_i), \quad (1)$$

where $g$ is the acceleration due to gravity, $\theta$ is the potential temperature, $u$ is the horizontal wind speed, $z$ is the height and the index $i$ refers to the model level. Between the surface and the lowest model level, the flux Richardson number was used due to problems with the bulk Richardson number. The mean vertical profiles of $Ri$ in the lowest 500 m over the fjords in the CONTROL simulations and NOTOPO simulations, shown in Fig. 9, clearly indicate that the topography had a large impact on the stability of the ABL. In all the fjords studied, $Ri$ was smaller in the CONTROL simulations meaning that the surrounding topography decreases the stability and enhances mixing over a fjord. The effect of the topography on the stability was most pronounced in the smallest fjord, Kongsfjorden.

Figure 10 shows the mean vertical profiles of potential temperature and specific humidity over Svalbard (D2 area) in the CONTROL simulations. The potential temperature always increased with the height but the humidity profiles were more complex and variable. Therefore, increased mixing due to the topography

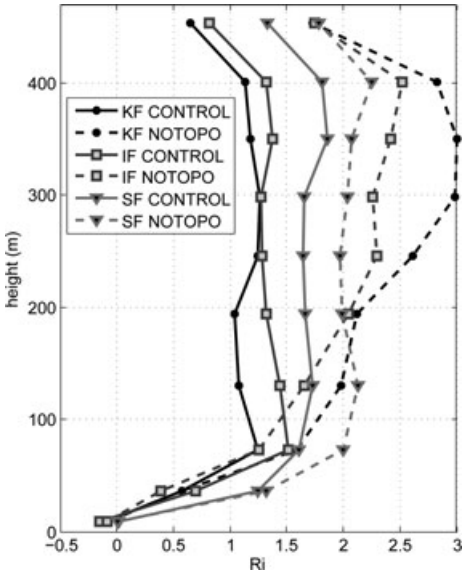


*Fig. 9.* The mean Richardson number (Ri) profiles over Storfjorden (SF), Isfjorden (IF) and Kongsfjorden (KF) in the CONTROL and NOTOPO simulations.

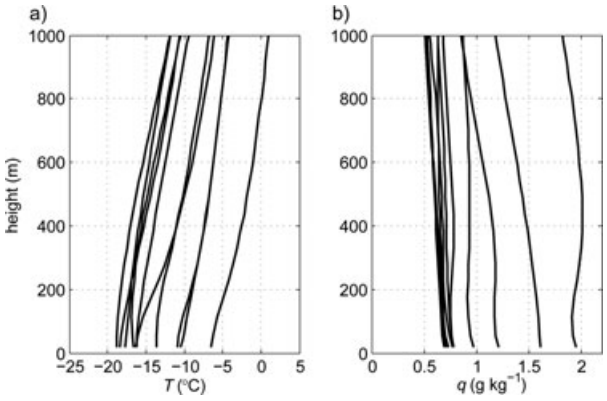


*Fig. 10.* The mean temperature $T$ and specific humidity $q$ profiles over Svalbard (D2 area) for 10 CONTROL simulations.

indicated by *Ri*-number (Fig. 9) led to higher near-surface temperatures but not always to moister near-surface conditions in the CONTROL simulations compared to the NOTOPO simulations, as seen in Figs 6–8. No clear evidence of mesoscale effects, for example, föhn, which could contribute to the warming effect was found in the simulations.

### 3.4. Comparison of effects of topography and surface type

In Fig. 11, the temporally averaged spatial standard deviation of the 10-m wind speed, 2-m temperature and specific humidity as well as the turbulent surface fluxes are shown for the CONTROL, NOICE, FULLICE and NOTOPO simulations. For wind speed, the difference in standard deviation between the CONTROL simulations and NOTOPO simulations was markedly larger than the difference between the CONTROL simulations and surface type sensitivity simulations, which means the effects of topography dominated over the effects of surface type. The influence of topography was larger in the SE case than in the NW due to higher wind speed. The results were similar for the momentum flux. The spatial variability of air temperature, specific humidity and the turbulent heat fluxes instead was clearly dominated by the effect of surface type. As expected, the effect of surface type was notably larger in the NW case than in the SE case due to low air temperature and large thermal contrasts. In the NW case, a partial sea ice cover increased the standard deviation by 2 °C for air temperature, 40–90 W $m^{-2}$ for the sensible heat flux and 20–40 W $m^{-2}$ for the latent heat flux.

### 3.5. Comparison of spatial and temporal variability

The spatial variability was compared to the temporal variability. The spatial and temporal standard deviations and their ratios in the CONTROL simulations are listed in Table 2. The spatial standard deviations were calculated taking a temporal average over the spatial standard deviations of the 10 cases simulated while the temporal standard deviations were calculated from the spatial averages of the 10 cases. The spatial variability of air specific humidity and temperature were least pronounced, but the other variables showed significant spatial variability that often reached levels comparable to the temporal variability. The ratio of spatial and temporal variability was generally largest in Isfjorden. The sensible heat flux seemed to be an exception with ratios decreasing with the fjord size and being very high (2.39) in Storfjorden.

The spatial and temporal standard deviations and their ratios for the NOTOPO simulations are listed in Table 3, analogously to the CONTROL simulations in Table 2. The spatial standard deviations were mainly smaller in the NOTOPO simulations compared to the CONTROL simulations, especially on a single surface type. The temporal variability, in turn, was often higher in the NOTOPO simulations, which was the case particularly for wind speed and temperature. As a consequence, the ratios between spatial variability and temporal variations were generally smaller in the NOTOPO (Table 3) than CONTROL simulations (Table 2), although also a few higher ratios were found especially in Kongsfjorden.

## 4. Discussion

The model validation against coastal observations in Isfjorden and Kongsfjorden revealed a systematic warm and moist bias and slightly overestimated wind speeds close to the surface. WRF's limited ability to simulate surface temperature inversions in the Arctic has been earlier reported, for example, by Mölders and Kramm (2009). In addition, our results resembled those based on validation of the ECMWF ERA-Interim reanalysis

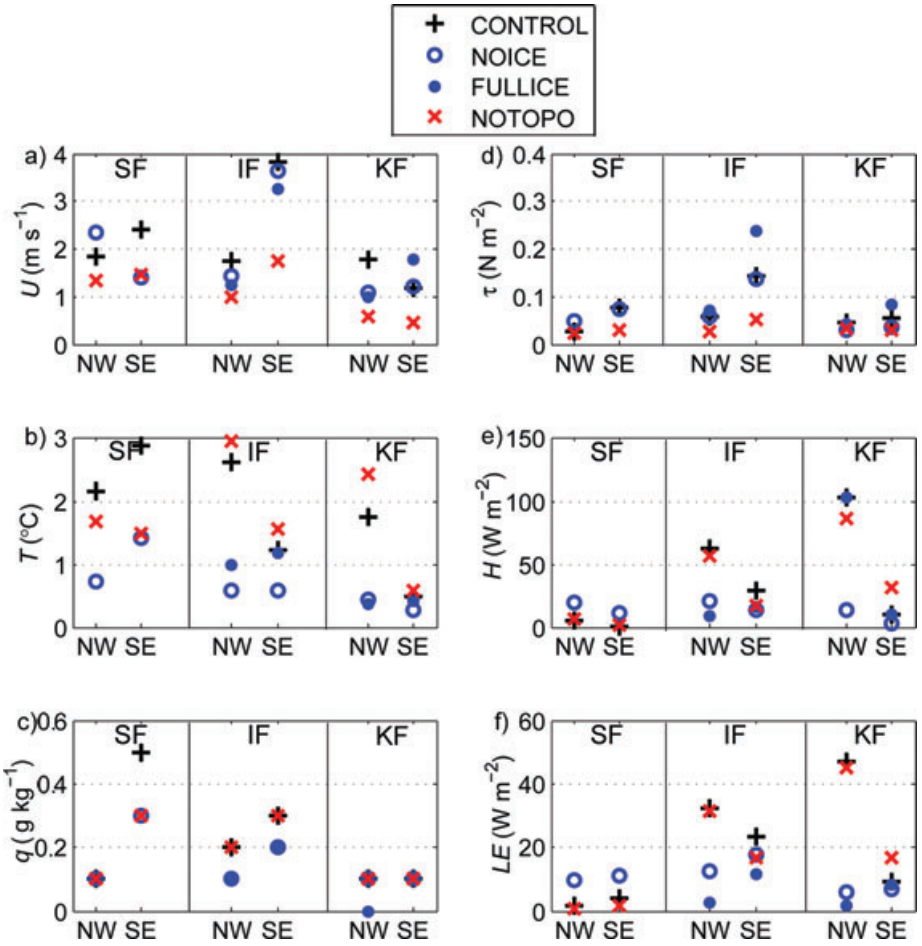


*Fig. 11.* The standard deviation of (a) 10-m wind speed $U$, (b) 2-m temperature $T$, (c) 2-m specific humidity $q$, (d) the momentum flux $\tau$, (e) the sensible heat flux $H$ and (f) the latent heat flux $LE$ for Storfjorden (SF), Isfjorden (IF) and Kongsfjorden (KF) in the CONTROL, NOICE, FULLICE and NOTOPO simulations on 19 February (NW) and 12 March (SE).

over the Arctic sea ice against (1) rawinsonde soundings made onboard R/V Polarstern during summers 1996, 2001 and 2007 (Lüpkes et al., 2010) and (2) tethersonde soundings made at the drifting ice station Tara in April–September 2007 [Erko Jakobson, personal communication, 2009; see also Vihma et al. (2008)]. All these model validations showed good wind profiles, a warm bias close to the ice surface, and a moist bias through the lowermost 1 km, indicating similar problems in WRF and ERA-Interim, which suggest for excessive mixing in the ABL. Also many regional climate models suffer from same kind of problems over the Arctic sea ice (Tjernström et al., 2005).

In the WRF results, the biases of the simulated variables were almost as large as the spatial standard deviations (Table 2). It is, however, well known that meteorological models perform better over a flat, homogeneous surface than over a coastline with complex topography. Further, models perform better for convective ABL than for SBL (Poulos and Burns, 2003). Kilpeläinen and Sjöblom (2010) concluded that under ice-free conditions in Isfjorden the Monin–Obukhov similarity theory, on which also the surface layer scheme used in this study is based, was more often valid when the flow was along the fjord than across the fjord. This suggests that the model performance is better in the middle parts of fjord where the flow is often channelled along the fjord. Hence, our model results were probably more accurate over the fjords, further away from the coastline and the topography, and especially over the open water areas than on the coastline where the validation was made. This gives a reason to trust that over the fjords the simulated spatial variability exceeded the model errors.

Skeie and Grønås (2000) suggested that a horizontal resolution of 10 km resolves the main topographic features of Svalbard, but, for example, Sandvik and Furevik (2002) as well as Skogseth et al. (2007) have emphasized the importance of a high horizontal resolution (2–4 km) for the modelling of the small-scale topographical features. Our results strongly support the need for the high horizontal resolution in an Arctic fjord environment, because the coarser resolutions (3 and 9 km) resulted to large deviations, reaching up to 50 W m$^{-2}$ for the turbulent heat

*Table 3*. Spatial (SPAT) and temporal (TEMP) standard deviations and their ratios for simulated 10-m wind speed ($U$), 2-m temperature ($T$), 2-m specific humidity ($q$), the momentum flux ($\tau$), the sensible heat flux ($H$) and the latent heat flux ($LE$) in Storfjorden (SF), Isfjorden (IF) and Kongsfjorden (KF) for the NOTOPO simulations. The number of grid points is given under the name

| | | SF fjord 1290 | IF fjord 3223 | IF water 2684 | IF ice 539 | KF fjord 277 | KF water 157 | KF ice 120 |
|---|---|---|---|---|---|---|---|---|
| SPAT($U$) | (m s$^{-1}$) | 1.5 | 1.1 | 1.1 | 1.0 | 0.7 | 0.7 | 0.3 |
| TEMP($U$) | (m s$^{-1}$) | 4.1 | 3.7 | 3.7 | 3.7 | 4.5 | 8.8 | 4.8 |
| **SPAT(U)/TEMP(U)** | | **0.37** | **0.29** | **0.29** | **0.27** | **0.15** | **0.08** | **0.06** |
| SPAT($T$) | (°C) | 1.2 | 2.3 | 0.8 | 0.5 | 1.7 | 0.4 | 0.1 |
| TEMP($T$) | (°C) | 6.0 | 3.6 | 3.4 | 4.9 | 3.6 | 3.1 | 4.5 |
| **SPAT(T)/TEMP(T)** | | **0.2** | **0.64** | **0.24** | **0.10** | **0.47** | **0.12** | **0.02** |
| SPAT($q$) | (g kg$^{-1}$) | 0.10 | 0.16 | 0.11 | 0.02 | 0.11 | 0.03 | 0.00 |
| TEMP($q$) | (g kg$^{-1}$) | 0.74 | 0.62 | 0.63 | 0.58 | 0.52 | 0.13 | 0.55 |
| **SPAT(q)/TEMP(q)** | | **0.14** | **0.26** | **0.17** | **0.03** | **0.21** | **0.23** | **0.00** |
| SPAT($\tau$) | (N m$^{-2}$) | 0.03 | 0.04 | 0.03 | 0.02 | 0.03 | 0.02 | 0.09 |
| TEMP($\tau$) | (N m$^{-2}$) | 0.10 | 0.13 | 0.13 | 0.10 | 0.15 | 0.23 | 0.12 |
| **SPAT($\tau$)/TEMP($\tau$)** | | **0.30** | **0.31** | **0.23** | **0.20** | **0.20** | **0.09** | **0.75** |
| SPAT($H$) | (W m$^{-2}$) | 6.7 | 59.8 | 21.1 | 7.4 | 95.7 | 14.2 | 3.2 |
| TEMP($H$) | (W m$^{-2}$) | 8.5 | 42.1 | 103.1 | 16.2 | 45.0 | 227.6 | 18.2 |
| **SPAT(H)/TEMP(H)** | | **0.79** | **1.42** | **0.20** | **0.46** | **2.13** | **0.06** | **0.18** |
| SPAT($LE$) | (W m$^{-2}$) | 1.6 | 32.8 | 7.2 | 1.9 | 41.8 | 6.1 | 0.7 |
| TEMP($LE$) | (W m$^{-2}$) | 2.8 | 34.3 | 40.6 | 4.1 | 30.0 | 100.0 | 3.8 |
| **SPAT(LE)/TEMP(LE)** | | **0.57** | **0.96** | **0.18** | **0.46** | **1.39** | **0.06** | **0.18** |

fluxes. Interestingly, the deviations of the means and standard deviations at coarser resolutions were not systematic for any particular variable, fjord or even surface type, meaning that the sign and magnitude of model bias caused by too coarse horizontal resolution were highly variable in the fjords and cannot therefore be generalized. Use of too coarse resolution simulations as boundary conditions for ocean modelling could therefore lead to erroneous current, water mass modification and ice production estimates, especially in smaller fjords like Isfjorden and Kongsfjorden. Nevertheless, the highest resolutions presently applied in operational NWP models for Svalbard are 4 and 8 km. These resolutions are not enough to capture all the complex small-scale processes which have an important role in the air–ice–sea interactions taking place in Arctic fjords.

The results of the multiple regression analyses suggested that spatial standard deviations for the wind speed and momentum flux were controlled by the mean wind speed, and for the temperature and specific humidity by the mean temperature. Expectedly, the spatial variability of temperature increased with the decreasing mean temperature, because low temperatures are usually connected to weaker winds and more stable conditions. In addition, even small changes in the turbulent heat fluxes can cause large changes in the temperature in the shallow SBL and therefore lead to large spatial variability. The temporally averaged local flux of momentum was mainly controlled by the wind speed, but also thermodynamic factors were important. This was the case particularly in Isfjorden, where the maximum momentum fluxes over the open water exceeded those over sea ice (Fig. 4), although the aerodynamic roughness of sea ice is larger. This demonstrates the dominating effects of unstable stratification on the vertical transfer of momentum. The local fluxes of sensible heat and latent heat were mainly controlled by thermodynamic factors instead of the wind speed.

The spatial variability of the near-surface variables has been studied over compact sea ice (Vihma et al., 2005), on the ice edge zone (Fairall and Markson, 1987; Brümmer et al., 2002) and around leads (e.g. Inoue et al., 2005), and found to be closely related to different surface types. Our results agreed that over partly ice-covered fjords, the different surface types substantially contributed to the amount of spatial variability, especially in the air temperature, specific humidity and the turbulent heat fluxes. The role of surface type increased with increasing air–temperature difference. However, the surrounding topography had also a large effect on the spatial variability of all the variables studied, and this effect was larger than the effects of surface type for wind speed and the momentum flux. The ratio between the topographic effects and the effects of surface type clearly depended on the air–sea temperature difference.

The topography of Svalbard generally increased the spatial variability of the near-surface variables and the turbulent fluxes, and often increased the temporal variability. Due to the topographic effects and strong stability of the flows, there could be

several air masses of different origin over a single fjord, leading to large spatial variability. In Isfjorden, the complex shape of the fjord seemed to hamper the efficient spreading of different air masses. The amount of spatial variability often varied with the large-scale flow directions, which represented different synoptic conditions, but also different topography in relation to the fjord orientation. The influence of topography on the mean values, in turn, was not systematic, although the results clearly indicated that the topography had a warming effect in all three fjords. The comparison of *Ri*-numbers showed that the topography enhanced the mixing in the ABL, which brought warmer air close to the surface from the layers above. This warmer air was not necessarily more humid, because the vertical specific humidity profiles were more complex than the potential temperature profiles. Hence, the effect of topography was consistent neither for specific humidity nor the latent heat flux.

The ratios between the spatial and temporal standard deviations indicated that the amount of spatial variability in a fjord can be comparable to the amount of temporal variability. It is well known and commonly emphasized that noticeable synoptic-scale variability takes place in the Arctic (Zhang et al., 2004; Nawri and Steward, 2009), causing drastic changes in the near-surface variables on a time scale of 1–3 d, or even shorter. Nevertheless, only a few studies have addressed both temporal and spatial variability of the near-surface variables and the turbulent surface fluxes or compared them over ice-covered seas. Brümmer et al. (2002) concluded, based on results from the ice edge zone in the Baltic Sea that the degree of spatial variability was dominated by the synoptic situation and was highest during cold-air advection. Our results showed that the importance of the spatial variability is pronounced in an Arctic fjord due to the topography. The ratios between the spatial and temporal standard deviations were smallest for the air temperature and specific humidity because they are relatively slowly reacting variables and largely influenced by the advection. The other variables, in turn, had notable spatial variations. The degree of temporal and spatial variability depended on the fjord size and shape. The synoptic conditions are seldom uniform over a large fjord like Storfjorden. On the other hand, Isfjorden has the most complex shape of all the three fjords studied which increased the spatial variations. In Kongsfjorden, the effect of topography is strongly present due to the small size of the fjord. Generally, many common features of spatial variability were found in the fjords studied but due to highly variable geography of fjords, all of the characteristics cannot be generalized to all Arctic fjords.

## 5. Acknowledgments

We are grateful to Marion Maturilli (Alfred Wegener Institute for Polar and Marine Research, Germany) for providing us with observations from Ny-Ålesund, Kongsfjorden. We also want to thank Stephanie Mayer, Marius Opsanger Jonassen, Teresa Valkonen and Keith M. Hines for their valuable help with the WRF model. The work of Timo Vihma was supported by the EC project DAMOCLES (grant 18509), which is a part of the Sixth Framework Programme.

## References

Andreas, E. L. 1987. Theory for the scalar roughness and the scalar transfer coefficients over snow and sea ice. *Boundary-Layer Meteorol.* **38**, 159–184.

Argentini, S., Viola, A. P., Mastrantonio, G., Maurizi, A., Georgiadis, T. and co-authors. 2003. Characteristics of the boundary layer at Ny-Ålesund in the Arctic during the ARTIST field experiment. *Ann. Geophys.* **46**, 185–196.

Barry, R. G. 2008. *Mountain Weather and Climate*. Cambridge University Press, Cambridge, 506 pp.

Bromwich, D. H., Hines, K. M. and Bai, L.-S. 2009. Development and testing of Polar Weather Research and Forecasting model: 2. Arctic Ocean. *J. Geophys. Res.* **114**(D08122), doi:10.1029/2008JD010300.

Brümmer, B., Schröder, D., Launiainen, J., Vihma, T., Smedman, A.-S. and co-authors. 2002. Temporal and spatial variability of surface fluxes over the ice edge zone in the northern Baltic Sea. *J. Geophys. Res.* **107**(C8), doi:10.1029/2001JC000884.

Chen, F. and Dudhia, J. 2001. Coupling an advanced land surface-hydrology model with the Penn State-NCAR MM5 modeling system. Part I: model implementation and sensitivity. *Mon. Wea. Rev.* **129**, 569–585.

Chou, M.-D. and Suarez, M. J. 1994. An efficient thermal infrared radiation parameterization for use in general circulation models. *NASA Tech. Memo.* 104606, 3, 85 pp.

Curry, J. A., Schramm, J. L., Alam, A., Reeder, R. and Arbetter, T. E. 2002. Evaluation of data sets used to force sea ice models in the Arctic Ocean. *J. Geophys. Res.* **107**(C10), 8027, doi:10.1029/2000JC000466.

Fairall, C. W. and Markson, R. 1987. Mesoscale variations in surface stress, heat fluxes, and drag coefficient in the marginal ice zone during the 1983 Marginal Ice Zone Experiment. *J. Geophys. Res.* **92**(C7), 6921–6932.

Grell, G. A. and Dévényi, D. 2002. A generalized approach to parameterizing convection combining ensemble and data assimilation techniques. *Geophys. Res. Lett.* **29**(14), 1693, doi:10.1029/2002GL015311.

Heinemann, G. and Klein, T. 2002. Modelling and observations of the katabatic flow dynamics over Greenland. *Tellus* **54A**, 542–554.

Heinemann, G. 2003. Forcing and feedback mechanisms between the katabatic wind and sea ice in the coastal areas of polar ice sheets. *J. Atmos. Ocean Sci.* **9**, 169–201.

Hines, K. M. and Bromwich, D. H. 2008. Development and testing of Polar Weather Research and Forecasting (WRF) model. Part I: Greenland ice sheet meteorology. *Mon. Wea. Rev.* **136**, 1971–1989.

Holtslag, A. A. M. and de Bruin H. A. R. 1988. Applied surface energy balance over land. *J. Appl. Meteorol.* **27**, 689–704.

Hong, S.-Y., Dudhia, J. and Chen, S.-H. 2004. A revised approach to ice microphysical processes for bulk parameterization of clouds and precipitation. *Mon. Wea. Rev.* **132**, 103–120.

Högström, U. 1988. Non-dimensional wind and temperature profiles in the atmospheric surface layer: a re-evaluation. *Boundary-Layer Meteorol.* **42**, 55–78.

Hunt, J. C. R., Shutts, G. J. and Derbyshire, S. H. 1996. Stably stratified flows in meteorology. *Dyn. Atmos. Oceans* **23**, 63–79.

Inoue, J., Kawashima, M., Fujiyoshi, Y. and Wakatsuchi, M. 2005. Aircraft observations of air-mass modification over the Sea of Okhotsk during sea-ice growth. *Boundary-Layer Meteorol.* **117**, 111–129.

Janjic, Z. I. 1996. The surface layer in the NCEP Eta model. *Eleventh Conference on Numerical Weather Prediction*, Norfolf, VA, 19-23 August, Amer. Meteor. Soc., Boston, MA, 354–355.

Janjic, Z. I. 2002. Nonsingular implementation of the Mellor-Yamada level 2.5 scheme in the NCEP Meso model. NCEP Office Note, **437**, 61 pp.

Kilpeläinen, T. and Sjöblom, A. 2010. Momentum and sensible heat exchange in an ice-free Arctic fjord. *Boundary-Layer Meteorol.* **134**, 109–130, doi:10.1007/s10546-009-9435-x.

Klein, T., Heinemann, G. and Gross, P. 2001. Simulation of the katabatic flow near the Greenland ice margin using a high-resolution nonhydrostatic model. *Meteorol. Z.* **10**, 331–339.

Klein, T. and Heinemann, G. 2002. Interaction of katabatic winds and mesocyclones at the eastern coast of Greenland. *Meteorol. Appl.* **9**, 407–422.

Launiainen, J. and Vihma, T. 1990. Derivation of turbulent surface fluxes—an iterative flux-profile method allowing arbitrary observing heights. *Environ. Software* **5**(3), 113–124.

Lüpkes, C., Vihma, T., Birnbaum, G. and Wacker, U. 2008. Influence of leads in sea ice on the temperature of the atmospheric boundary layer during polar night. *Geophys. Res. Lett.* **35**(L03805), doi:10.1029/2007GL032461.

Lüpkes, C., Vihma, T., Jakobson, E., König-Langlo, G. and Tetzlaff, A. 2010. Meteorological observations from ship cruises during summer to the central Arctic: a comparison with reanalysis data. *Geophys. Res. Lett.* **37**(L09810), doi:10.1029/2010GL042724.

Mlawer, E. J., Taubman, S. J., Brown, B. D., Iacono, M. J. and Clough, S. A. 1997. Radiative transfer for inhomogeneous atmospheres: RRTM, a validated correlated-k model for the longwave. *J. Geophys. Res.* **102**(D14), 16663–16682.

Mölders, N. and Kramm, G. 2009. A case study on wintertime inversions in Interior Alaska with WRF. *Atmos. Res.* **95**, doi:10.1016/j.atmosres.2009.06.002.

Nawri, N. and Steward, R. E. 2009. Short-term temporal variability of the atmospheric surface pressure and wind speed in the Canadian Arctic. *Theor. Appl. Climatol.* **98**, 151–170.

Ohigashi, T. and Moore, G. W. K. 2009. Fine structure of a Greenland reverse tip jet: a numerical simulation. *Tellus* **61A**, 512–526.

Poulos, G. S. and Burns, S. P. 2003. An evaluation of bulk Ri-based surface layer flux formulas for stable and very stable conditions with intermittent turbulence. *J. Atmos. Sci.* **60**, 2523–2537.

Sandvik, A. D. and Furevik, B. R. 2002. Case study of a coastal jet at Spitsbergen – comparison of SAR- and model-estimated wind. *Mon. Wea. Rev.* **130**, 1040–1051.

Skeie, P. and Grønås, S. 2000. Strongly stratified easterly flows across Spitsbergen. *Tellus* **52A**, 473–486.

Skamarock, W. C., Klemp, J. B., Dudhia, J., Gill, D. O., Barker, D. M. and co-authors. 2008. A description of the Advanced Research WRF version 3. NCAR Technical Note – 475+STR.

Skogseth, R., Sandvik, A. D. and Asplin, L. 2007. Wind and tidal forcing on the meso-scale circulation in Storfjorden, Svalbard. *Cont. Shelf Res.* **27**, 208–227.

Skogseth, R., Smedsrud, L. H., Nilsen, F. and Fer, I. 2008. Observations of hydrography and downflow of brine-enriched shelf water in the Storfjorden polynya, Svalbard. *J. Geophys. Res.* **113**(C08049), doi:10.1029/2007JC004452.

Tisler, P., Vihma, T., Müller, G. and Brümmer, B. 2008. Modelling of warm-air advection over Arctic sea ice. *Tellus* **60A**, 775–788.

Tjernström, M., Zagar, M., Svensson, G., Cassano, J. J., Pfeifer, S. and co-authors. 2005. Modelling the Arctic boundary layer: an evaluation of six ARCMIP regional-scale models using data from the SHEBA project. *Boundary-Layer Meteorol.* **117**, 337–381.

Valkonen, T., Vihma, T. and Doble, M. 2008. Mesoscale modeling of the atmosphere over Antarctic sea ice: a late autumn case study. *Mon. Wea. Rev.* **136**, 1457–1474.

Valkonen, T., Vihma, T., Kirkwood, S. and Johansson, M. M. 2010. Fine-scale model simulation of gravity waves generated by Basen nunatak in Antarctica. *Tellus* **62A**, 319–332, doi:10.1111/j.1600-0870.2010.00443.x.

Vihma, T., Uotila, J., Cheng, B. and Launiainen, J. 2002. Surface heat budget over the Weddel Sea: buoy results and model comparison. *J. Geophys. Res.* **107**(C2), 3013, doi:10.1029/2000JC000372.

Vihma, T., Hartmann, J. and Lüpkes, C. 2003. A case study of an on-ice air flow over the Arctic marginal sea-ice zone. *Boundary-Layer Meteorol.* **107**, 189–217.

Vihma, T., Lüpkes, C., Hartmann, J. and Savijärvi, H. 2005. Observations and modelling of cold-air advection over Arctic sea ice. *Boundary-Layer Meteorol.* **117**, 275–300.

Vihma, T., Jaagus, J., Jakobson, E. and Palo, T. 2008. Meteorological conditions in the Arctic Ocean in spring and summer 2007 as recorded on the drifting station Tara. *Geophys. Res. Lett.* **35**(L18706), doi:10.1029/2008GL034681.

Zhang, X., Walsh, J. E., Zhang, J., Bhatt, U. S. and Ikeda, M. 2004. Climatology and interannual variability of Arctic cyclone activity: 1948-2002. *J. Climate* **17**, 2300–2317.

Zilitinkevich, S. S. and Esau, I. N. 2005. Resistance and heat-transfer laws for stable and neutral planetary boundary layers: old theory advanced and re-evaluated. *Quart. J. R. Meteorol. Soc.* **131**, 1863–1892.